



Deflectometry based calibration of a deformable mirror for aberration correction and remote focusing in microscopy

KENTA TEMMA,¹ MATTHEW WINCOTT,² KATSUMASA FUJITA,¹  AND MARTIN J. BOOTH^{2,*} 

¹Department of Applied Physics, Osaka University, Suita, Osaka 565-0871, Japan

²Department of Engineering Science, University of Oxford, Parks Road, Oxford OX1 3PJ, UK

*martin.booth@eng.ox.ac.uk

Abstract: Adaptive optics (AO) techniques enhance the capability of optical microscopy through precise control of wavefront modulations to compensate phase aberrations and improves image quality. However, the aberration correction is often limited due to the lack of dynamic range in existing calibration methods, such as interferometry or Shack-Hartmann (SH) wavefront sensors. Here, we use deflectometry (DF) as a calibration method for a deformable mirror (DM) to extend the available range of aberration correction. We characterised the dynamic range and accuracy of the DF-based calibration of DMs depending on the spatial frequency of the test pattern used in DF. We also demonstrated the capability of large magnitude phase control for remote-focusing over a range larger than was possible with SH sensing.

Published by Optica Publishing Group under the terms of the [Creative Commons Attribution 4.0 License](https://creativecommons.org/licenses/by/4.0/). Further distribution of this work must maintain attribution to the author(s) and the published article's title, journal citation, and DOI.

1. Introduction

Optical microscopy benefits from the use of adaptive optics (AO) for correction of aberrations arising from the non-homogeneous refractive index of specimens [1,2]. AO can also be used for other functionality, such as beam-shaping, point spread function engineering, and remote focusing. Re-configurable devices, such as a deformable mirror (DM), or spatial light modulator, are used to modify the wavefront of the illumination or emission light to compensate specimen-induced aberrations or to impart other wavefront modulations, such as refocusing. The performance of these systems relies on the precise control of the wavefront modulations created by the adaptive devices, which in turn requires an effective calibration process [3,4].

Calibration of AO devices is often performed using an interferometer [5] or Shack-Hartman (SH) wavefront sensor [6,7], which can readily measure to precisions much smaller than a wavelength. However, the dynamic range of these measurements for each sensor design is limited and a change in range would require reconfiguration. For example, calibration of remote focusing [8–12], where a defocus mode is applied to the AO device to adjust the focus position without mechanical scanning, requires measurement over many wavelengths. Measurement of such large phase variations is often beyond the capabilities of practical interferometry or SH sensing.

In this paper, we report on the use of deflectometry (DF) as a calibration method for a DM to extend the available range of aberration correction. DF utilizes patterned light (typically comprising a sinusoidal test pattern) observed via a non-flat reflective surface. The patterned light, when captured by a camera, is distorted by the local shape of the surface. The shape of the sample surface can be retrieved through analysis of the distorted light pattern [13–18]. Furthermore, the only hardware required for DF is a display for projecting fringe patterns and a camera, which leads to a simpler implementation compared to conventional calibration methods.

We investigated the effectiveness of DF for the calibration of a DM, characterised in terms of dynamic range and accuracy depending on the spatial frequency of the test pattern. We applied the DF-based calibration system to adaptive widefield-sectioning fluorescence microscopy. Demonstrations of remote-focusing combined with aberration correction verified the capability for large-magnitude phase control.

2. Theoretical explanation of deflectometry on a deformable mirror

Deflectometry can measure the surface shape of a DM through the distortions of a structured illumination pattern (which we refer to here as the fringe pattern) viewed on a camera via the DM. The fringe pattern is typically chosen to be a sinusoidal variation in intensity, which is produced by a display device, such as a light emitting diode or liquid crystal display panel. The image of the fringe pattern is distorted by the shape of the DM. Essentially, the local displacement of the pattern is proportional to the local gradient of the DM surface. While the theory of deflectometry is well documented elsewhere [15], we reproduce here for convenience the derivations necessary for DM calibration.

Consider a light ray that is reflected at a point on a flat reference surface of the DM (Fig. 1). If the surface is tilted locally to have an angle of θ from flat, this introduces an additional 2θ deflection, resulting in an apparent shift at the detector. The displacement δ from the reference

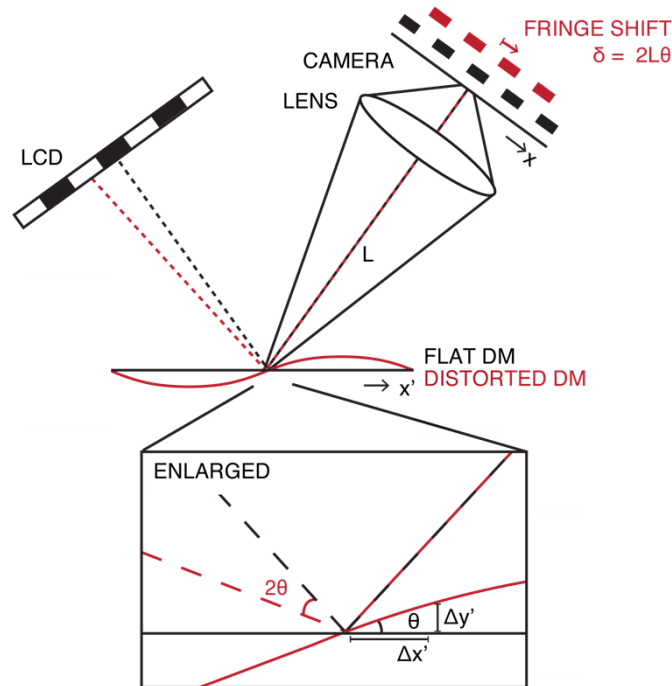


Fig. 1. Principle of deflectometry. A one-dimensional fringe pattern was assumed for the purposes of illustration. A point in a deformable mirror surface with a local slope of θ reflects the fringe pattern. δ is zero when the reflection surface is flat. $\Delta x'$ and $\Delta y'$ are local base and height of a deformable mirror forming an angle θ . Red and black dotted line show representative chief rays propagated back to the LCD in case of tilted and normal surface, respectively.

position at the detector plane is obtained as

$$\delta = L \tan 2\theta \cong 2L\theta \quad (1)$$

where L is the distance between a reflection point and the detector plane. It was assumed that the angle θ was small. Considering a fringe pattern that varies in the x direction, the distribution of the patterned light at the detection plane can be expressed as

$$I(x) = a + b \cos(2\pi fx) \quad (2)$$

where a is the background at the detection plane. b and f are the amplitude and frequency of the fringe pattern. x is the horizontal coordinate in the detector plane. When the pattern is distorted by the non-flat DM surface, the fringe pattern at the detector plane becomes

$$I(x) = a + b \cos\{2\pi f(x + 2L \theta(x'))\} \quad (3)$$

The local phase of the fringe pattern was changed due to the reflection at the deformed surface with a local surface angle of $\theta(x')$. Assuming that $\theta(x')$ varies sufficiently slowly, the relationship between local gradient and spatial phase shift of the fringe pattern can be obtained as

$$\Delta\phi = 4\pi fL \theta(x') \quad (4)$$

The purpose of the calibration exercise is to obtain the optical phase modulation from the deflectometry measurement. The optical phase shift $\Delta\psi$ imparted by a deformable mirror with displacement $\Delta y'$ is obtained as,

$$\Delta\psi = 2\pi/\lambda (2\Delta y') \quad (5)$$

where λ is the wavelength. Note the factor of 2, as the optical path length change is twice the displacement of the DM. The phase gradient is determined as the differentiation of the local height

$$d\psi/dx' = 4\pi/\lambda dy'/dx' = 4\pi/\lambda \theta(x') \quad (6)$$

Combining Eq. (4) with Eq. (6), we obtain

$$d\psi/dx' = \Delta\phi/\lambda fL \quad (7)$$

In the practical measurement and reconstruction process, the fringe pattern is magnified and sampled by a detector with pixel spacing p . The fringe period, which is equivalently the reciprocal of the frequency, is given by $\frac{1}{f} = Mp$, where M represents the number of pixels per fringe. In a similar way, we can represent the coordinate at the detector as $x = Xp$, where X is the pixel index. Equation (7) can hence be rewritten in terms of pixel indices, rather than real coordinates, as

$$d\psi/dX = \phi Mp^2/\lambda L \quad (8)$$

To retrieve the phase using Zernike polynomials [19], the coordinate should be normalized, so that the pupil is defined as the unit circle. Hence, we use the coordinate $r = X/\rho$, where ρ is the radius of the pupil in pixels. Then, the phase gradient obtained by deflectometry can be expressed as

$$d\psi/dr = \phi M\rho p^2/\lambda L \quad (9)$$

Hence the gradient of the wavefront phase ψ in the direction of the fringe pattern variation can be obtained from the phase ϕ retrieved from the fringe pattern. If the fringe patterns are acquired

with orthogonal orientations, for example along the x and y axes, then the phase ψ can be obtained through joint integration with respect to x and y . Integration is carried out with modal-based estimation of Zernike coefficients by using the derivatives of Zernike polynomials [20,21].

In the following measurements, we used a two-dimensional fringe pattern to obtain simultaneously the phase gradient in orthogonal directions [22]. The phase of the fringe pattern was retrieved by analysis in the Fourier domain [23]. The details of analysis procedure are explained in [Supplement 1](#).

3. Experimental systems for deflectometry characterisation

Two different DMs were characterized using deflectometry through two different optical systems, denoted here as system A and system B (Fig. 2).

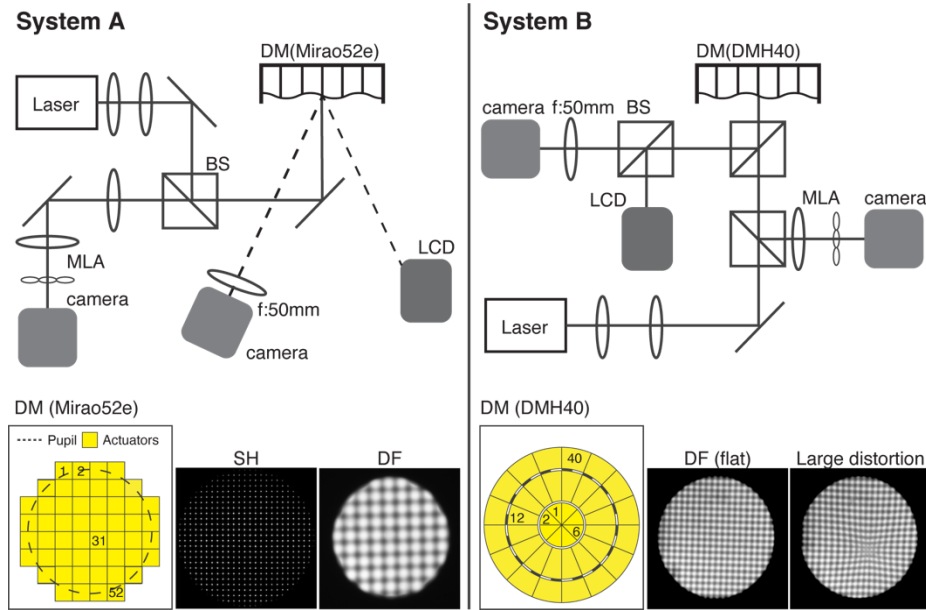


Fig. 2. Optical set-ups for deflectometry characterization. (DM: Deformable mirror, BS: Beam splitter, MLA: Microlens array, LCD: Liquid crystal display). Maps of actuators are shown for the DMs in each system; some actuator indices have been provided. On the left, example experimental images are presented, as obtained by the Shack-Hartmann wavefront sensor (SH) and Deflectometry (DF). On the right, DF images with near-flat DM surface and large distortion are shown for the illustration of the DF measurement process.

In system A, the fringe pattern was generated on a liquid crystal display (LCD) (Pico-ResTouch-LCD-3.5, Waveshare) and imaged onto the camera via the surface of a deformable mirror (Mirao52e, Imagine Optic). The reflected fringe pattern was taken by a CMOS camera (xiQ, ximea), whose pixel size was $4.8 \mu\text{m} \times 4.8 \mu\text{m}$ located at 430 mm from the DM. The camera was focused on the DM. Measurements were quantified in terms of optical path length in order to avoid the ambiguity of wavelength of the LCD source. The full range of control voltages used by the DM was 0 to +1.0 V. We also performed simultaneous measurement with the Shack-Hartmann wavefront sensor (WFS20-7AR/M, Thorlabs) employing a 632.8 nm CW laser as the source. A micro-lens array consisting of lenses with a focal length of 5.2 mm arranged in square grid in a $150 \mu\text{m}$ pitch was used for separating pupil into foci. The image in Fig. 2 shows the spot pattern from the SH sensor.

In system B, fringe patterns were generated on the LCD and imaged via the deformable mirror (DMH40/M-P01, Thorlabs). A CMOS camera (xiC, ximea) with a pixel size of $5.86\ \mu\text{m} \times 5.86\ \mu\text{m}$ was focused on the surface of a deformable mirror to capture the reflected fringe pattern. The distance between the DM and the camera was 450 mm. The full range of control voltages used by the DM was 0 to 1.0 V.

4. Controlling dynamic range through fringe frequency

We investigated the dependence of the dynamic range of deflectometry measurement on the frequency of the applied fringe patterns. Figure 3 shows the influence functions of a single actuator of the deformable mirror, which is the wavefront formed when a single actuator was driven with the stated control voltage. Influence functions were measured by deflectometry with fringe patterns of three different frequencies (quantified as 20, 10, and 5 periods across the DM diameter). The example shown used an actuator located near the center of DM (number 31), which was driven with different control voltages between 0.505 to +1.0 V. A uniform application of control voltages of 0.5 V provided nearly flat DM surface.

Reconstruction results indicated that the high-frequency pattern allowed retrieval of the wavefront shape for small deflections, but it was not capable of retrieving the large deformations when the mirror was driven with voltages between 0.8 to 1.0 V. This is presumably because the large distortion degraded the contrast of fringe pattern, as shown in Fig. 3, which made it difficult to retrieve the phase gradient information. Using low frequency patterns, it was possible to retrieve the larger mirror deformations. On the other hand, the lower frequency patterns led to errors in the measurement for small deformations at 0.51 V. This illustrates the trade-offs between range and precision using deflectometry for DM characterization.

Overall in these measurements, the medium frequency pattern provided a compromise performance between dynamic range and precision. These results also indicated that we can arbitrarily change the range of measurement by using different fringe patterns dependent on the application.

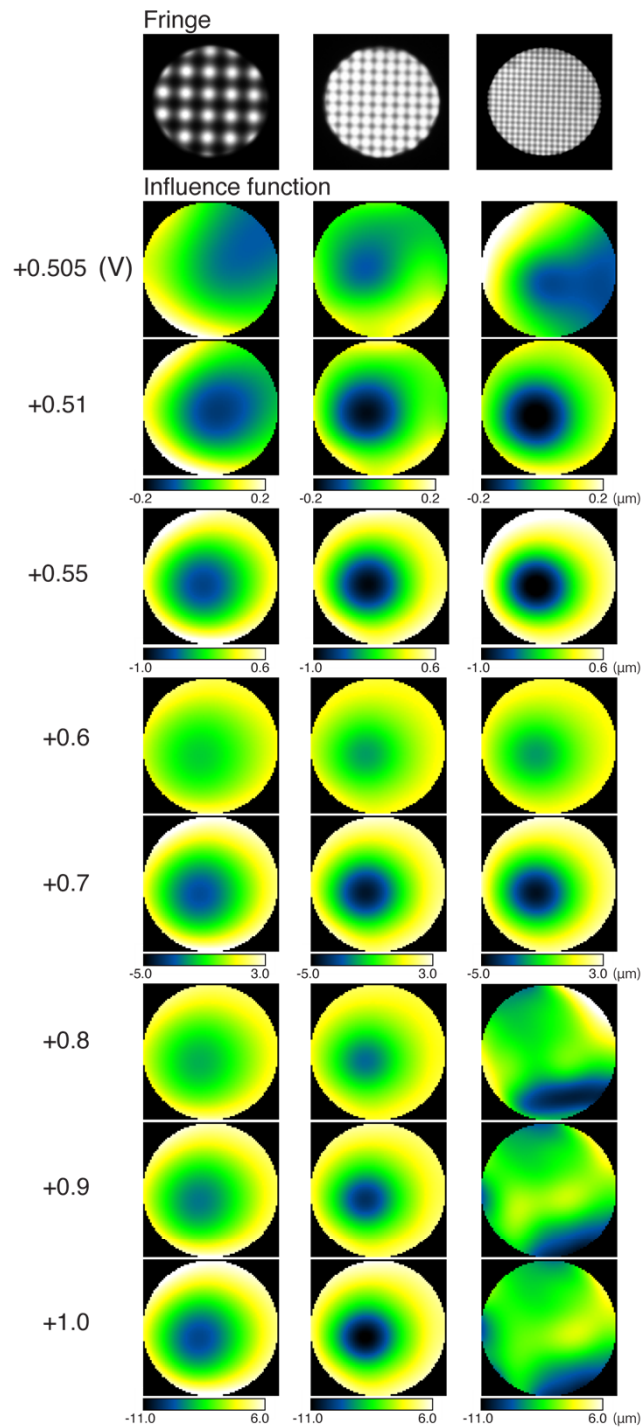


Fig. 3. Influence functions of the Mirao52e deformable mirror measured by deflectometry with fringe patterns of three different frequencies. The applied fringe patterns are shown at the top. A single actuator (number 31) was driven at different control voltages. Applied voltages are shown on the left.

5. Measurement accuracy with different fringe patterns

We evaluated the dependence of the accuracy of the deflectometry measurement on the frequency of the fringe pattern with reference to measurement by the SH sensor. For this measurement we used system B. Influence functions of a single actuator driven at fixed control voltage (1.0 V) were measured by deflectometry with fringe patterns of different frequencies. We also measured the same surface with the SH sensor. Two actuators were used for this comparison: the first (*act6*) was located near the center of the DM; the second (*act12*) was at the edge of DM (see Fig. 2). This enabled observation of the difference in accuracy due to the position of the mirror deformation. The SH sensor was used for the reference measurement for all cases. It should be noted that this measurement itself may be subject to error, as discussed later.

Figure 4 shows the retrieved wavefronts obtained with both methods. It was observed that in most cases the deflectometry derived measurements matched closely the SH reference. There were significant errors in the deflectometry measurement when using the high-frequency pattern for *act6*. In this case, the measurement failed to provide an accurate measurement due to the dynamic range issues discussed above. The accuracy was quantified by calculating the root mean

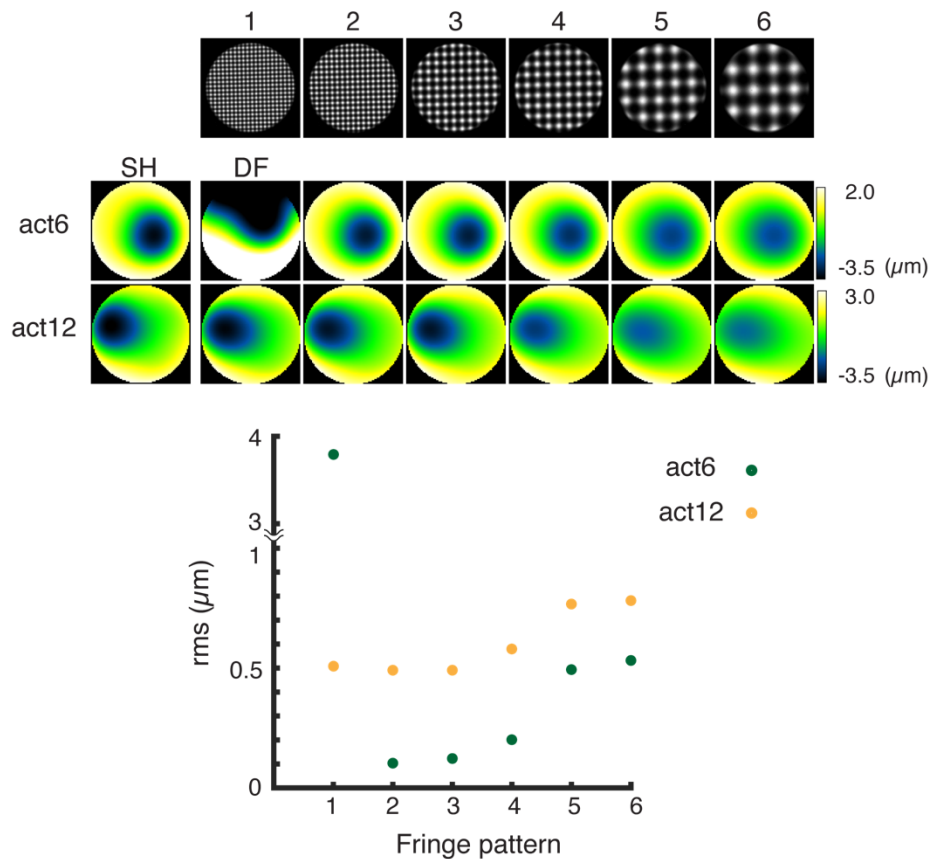


Fig. 4. Influence functions measured by Shack-Hartmann (SH) wavefront sensor and deflectometry (DF). Different fringe patterns with frequencies (measured in periods per DM diameter) of 22, 17, 11, 9, 6, 4 for patterns 1 to 6, respectively, were used for the deflectometry measurement. The two actuators (*act6* and *act12*) were located at the center and edge of the deformable mirror. The root-mean-square value of the difference between the SH and DF measurement was plotted.

square error between the deflectometry and the SH measurements, which was calculated as,

$$rms = \sqrt{\sum_{i=1}^N [W_{DF}(i) - \{W_{SH}(i) - s\}]^2 / N} \quad (10)$$

where N is the number of pixels inside the pupil of an influence function. The influence functions obtained by SH ($W_{SH}(i)$) were subtracted from the DF results ($W_{DF}(i)$) in each actuator and root mean square values were calculated. The difference of offset due to the piston (s) was compensated before subtraction. The general trend showed that the accuracy was worse with fringe patterns of lower frequency.

For *act6*, the optimum performance was obtained at a similar accuracy for patterns 2, 3 and 4. For *act12*, the optimum performance was found for pattern 3, although the accuracy overall was lower than for *act6*. This may be a consequence of using the SH measurement as a reference. The SH measurement relies on segmenting the pupil with the microlens array. This means that deformations at the edge of the pupil may not be adequately sampled and hence the SH retrieved wavefront may not be as accurate for *act12* as it was for *act6*. The phase retrieval for *act6* and pattern 1 failed due to loss of pattern contrast in this case for the finer pattern.

These results indicate that the choice of fringe pattern plays an important role in balancing accuracy and range when using deflectometry to characterize the DM.

6. Calibration of remote focusing in microscopy

An adaptive fluorescence microscope system was constructed in order to demonstrate the aberration correction and remote focusing capability of a deflectometry-calibrated DM. Remote focusing requires the calibration of a DM over a large range of wavefront deformations. As a large dynamic range is required, it is difficult to perform this calibration task using SH sensors or interferometry. For this reason, it is useful to assess the capability of deflectometry to perform this characterization task.

The adaptive microscope system used an aperture correlation spinning disk microscope that provided optical sectioning capability in widefield fluorescence imaging (Clarity, Aurox Ltd.) [24,25]. The Clarity microscope contained a spinning disk that incorporated striped patterns that created structured illumination and structurally filtered detection. Two images – one passing through the disk and one reflected off the disk, were captured by the camera and processed to obtain an optically sectioned image. The spinning disk was placed at the intermediate image plane both in excitation and emission paths. In the excitation path, the spinning disk generated the structured illumination pattern at the focus plane. Fluorescence emission passed through or was reflected by the spinning disk in the detection path. The transmitted and reflected images were processed to reject the out-of-focus light and create the optically sectioned image. The optical set-up shown in Fig. 5 was similar to the one developed in Ref. [26], with the addition of the deflectometry calibration system. A LED source (PE 300 Ultram CoolLED) was connected through the Clarity unit. The DM (Mirao52e, Imagine Optics) was inserted in an intermediate pupil plane using 4f relay optics between the Clarity module and the microscope. This was constructed using a pair of achromatic doublets with a focal length of 300 mm. In this position, the DM corrected both the illumination and detection paths simultaneously. Illumination light entered the microscope body (iX71, Olympus) and was focused by an 60× oil immersion objective lens with an NA of 1.4 (PlanApo, Olympus). The axial position of the objective lens was controlled by a piezo actuator (P-736.SRIS, PI-nano Z Microscope Scanner, Physik Instrumente). Fluorescence signals were collected by the same objective and imaged at the camera (Prime BSI, Photometrics). Excitation and emission wavelengths could be selected by choosing a dichroic filter in Clarity. We used two types of filters, (Ex 554 nm FWHM 23 nm/Em 609 nm FWHM 54 nm) and (Ex 578 nm FWHM 21 nm/Em 641 nm FWHM 75 nm) in the following experiments. A deflectometry-based calibration system similar to system A was included in the set-up. The LCD and CMOS camera

(xiQ, ximea, pixel size: $4.8 \mu\text{m} \times 4.8 \mu\text{m}$) were arranged at an angle of 34° so as not to interfere with the optical path of the microscope. The distance between DM and the camera was 430 mm.

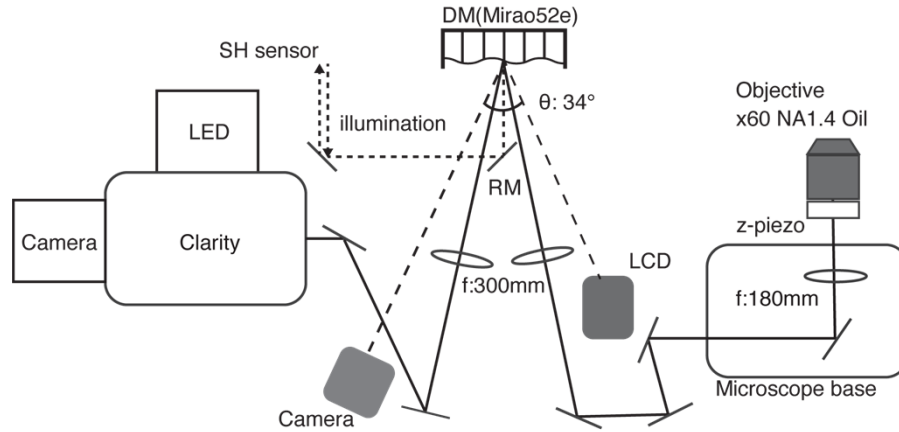


Fig. 5. Optical set-up of the adaptive fluorescence microscope (RM: Removable mirror).

We conducted remote-focusing fluorescence microscopy with the deflectometry-calibrated DM, where the calibration was undertaken using fringe pattern with a frequency of 20 fringes per diameter. Figure 6(a) shows the fluorescence images of $1 \mu\text{m}$ beads at the depth of $-50 \mu\text{m}$ to $50 \mu\text{m}$. The position of the objective lens was moved to each depth with the piezo actuator. A pre-calculated amount of the defocus mode was applied to the DM to adjust the focus approximately to the desired position. This pre-adjustment reduced the demands on the next calibration step when other aberration modes were adaptively optimised. At the deeper region, the effect of higher order spherical aberration modes became large, so an estimated amount of these modes was also applied in advance [27]. Following this, modal based sensor-less AO was applied in order to optimise aberration modes including defocus. The sensor-less correction effectively found the remaining system aberration by maximising an image quality metric through application of different amplitudes of aberration modes [28,29]. In a correction cycle, we used Zernike modes of defocus, 1st and 2nd order spherical, astigmatism, coma, and trefoil. In this process, the optimization metric was defined as the mid-high spatial frequency signals of the image, as these are most affected by aberrations [26]. The highest frequency used for the metric was defined as $\frac{2NA}{1.22\lambda}$ ($3.8 \mu\text{m}^{-1}$) and the lowest frequency was 10% of the highest frequency. In this range, the sum of the signals above the noise level was used as the metrics. The noise level was defined as 1.125 times the mean of the signals above the frequency of 1.1 times the defined cutoff frequency ($4.14 \mu\text{m}^{-1}$). The correction cycle was repeated three times. The reduction in image brightness at the larger displacements from $0 \mu\text{m}$ was attributed to the residual spherical aberration arising from small amounts of the 3rd spherical aberration term that was not included in the correction cycle. Although the brightness monotonically decreased to about 40% of the maximum, spatial resolution does not follow the same tendency. Spatial resolution was maintained between -30 to $30 \mu\text{m}$. Even at greater depth, it was not severely degraded.

Following this calibration, we measured the wavefront deformation introduced by the DM through deflectometry and the SH wavefront sensor when the pre-determined remote-focusing calibrations were applied. In Fig. 6(b), reconstructed wavefront shapes for $+10$ to $+50 \mu\text{m}$ remote-focusing are shown. These results clearly illustrate the inability of the SH sensor to retrieve the shape above $+30 \mu\text{m}$ focusing due to its limited dynamic range. On the other hand,

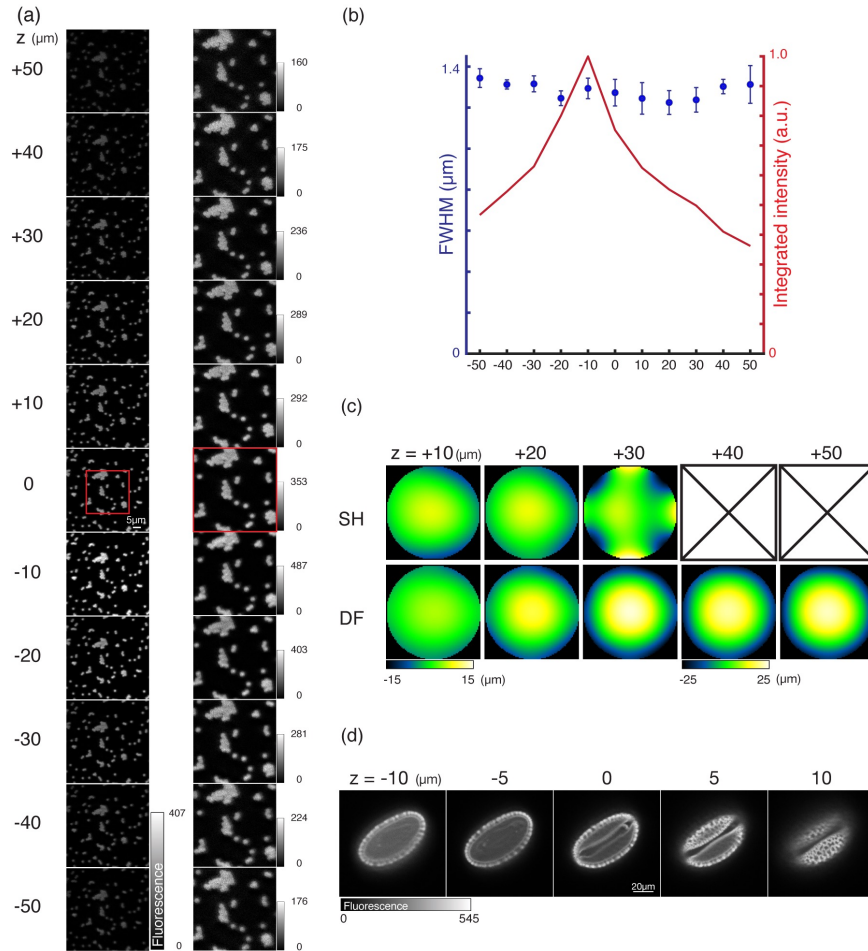


Fig. 6. (a) Fluorescence images of 1 μm beads with aberration correction and remote focusing between $-50\text{ }\mu\text{m}$ and $50\text{ }\mu\text{m}$. The fluorescence signal was obtained with a dichroic filter (Ex 554 nm FWHM 23 nm/Em 609 nm FWHM 54 nm). Illumination power after the objective lens (60 \times , NA 1.4, Oil) was 0.515 μW . Exposure time was 100 ms. (b) Averaged FWHM of five fluorescent beads and normalized integrated intensity of fluorescence images at different imaging depth. (c) Wavefront shapes introduced by the deformable mirror, measured with SH wavefront sensor and DF. For these measurements, the modes for remote focusing between +10 to +50 μm were applied to the deformable mirror. The SH sensor failed to retrieve accurately the wavefronts for larger deformations. (d) Fluorescence images of pollen grain through remote-focusing over $-10\text{ }\mu\text{m}$ to $10\text{ }\mu\text{m}$ axial slices. The fluorescence signal was obtained with a dichroic filter (Ex 578 nm FWHM 21 nm/Em 641 FWHM 75 nm). Illumination power after the objective lens (60 \times , NA 1.4, Oil) was 7.8 μW . Exposure time was 120 ms.

DF succeeded to measure the shape of $+50\ \mu\text{m}$ focusing which is the maximum available stroke of the DM.

We also demonstrated remote-focusing imaging of pollen grain that has a relatively thick and dense structure compared to beads in Fig. 6(d). We used pre-calibrated shapes of deformable mirror that was obtained in the fluorescence beads measurements at each depth. We confirmed that remote focusing under this calibration can be applied to a volumetric specimen.

7. Discussion and conclusion

We have investigated the use of deflectometry for the calibration of a deformable mirror for application to aberration correction and remote focusing for microscopy. We confirmed that the dynamic range for measuring the influence function of the single actuator in a deformable mirror can be tuned by changing the frequency of the fringe pattern. We compared the relative measurement accuracy of deflectometry with different frequency fringe patterns compared to Shack-Hartmann measurements. Higher frequency patterns provided results comparable to that of the SH. On the other hand, the error was larger for lower frequency patterns. It was found that the dynamic range of the deflectometry measurement was tunable, with a trade-off for measurement accuracy. Hence, the fringe pattern should be determined to fit to the purpose of the calibration.

Considering the general requirements for DF imaging systems, a camera with a smaller pixel size would be useful to measure finer fringe patterns and improve measurement accuracy. Low detection noise is also desirable for fringe analysis and phase retrieval processes. However, the required specification of the imaging system depends strongly on the purpose of the calibration. Hence, design compromises were possible in this application. We know the spatial scale of distortions on the DM as it is determined by the actuator spacing. Hence, it is not necessary for the system to have a spatial resolution significantly finer than the actuator spacing. Furthermore, there is some flexibility on the positioning of the camera focus, which could possibly be anyway between the DM and the display device.

We performed remote-focusing fluorescence microscopy to verify the extension of wavefront control dynamic range. Fluorescence beads defocused in the range of -50 to $50\ \mu\text{m}$ were effectively re-focused by the deformable mirror. While deflectometry was able to measure the large refocusing wavefront deformation, it was not possible to measure over the same large range with SH sensing.

A major advantage of deflectometry is its simple configuration, as it more straightforward to incorporate into an existing adaptive microscope system than other methods, such as SH sensing or interferometry. Such in-situ monitoring of the DM can help implementation of feedback control to deal with issues such as drift or creep [30]. It could particularly be applied to compensate for the hysteresis of low-cost piezo actuator-based DMs, thus making such adaptive optics methods more widely usable.

Funding. European Research Council (695140); Core Research for Evolutional Science and Technology (JPMJCR1925).

Acknowledgment. The authors thank Dr. Qi Hu for help with sample preparation.

Disclosures. The authors declare no conflicts of interest.

Data availability. Data underlying the results presented in this paper are not publicly available at this time but may be obtained from the authors upon reasonable request.

Supplemental document. See [Supplement 1](#) for supporting content.

References

1. M. J. Booth, "Adaptive optics in microscopy," *Philos. Trans. R. Soc., A* **365**(1861), 2829–2843 (2007).
2. M. J. Booth, "Adaptive optical microscopy: the ongoing quest for a perfect image," *Light: Sci. Appl.* **3**(4), e165 (2014).

3. M. Booth, T. Wilson, H. Sun, T. Ota, and S. Kawata, "Methods for the characterization of deformable membrane mirrors," *Appl. Opt.* **44**(24), 5131–5139 (2005).
4. J. Antonello, J. Wang, C. He, M. A. Phillips, and M. J. Booth, "Interferometric calibration of a deformable mirror," DOI: 10.5281/zenodo.3714951, <https://aomicroscopy.org/dm-calib>.
5. M. Born and E. Wolf, *Principles of Optics* (Cambridge University Press, 1999).
6. B. C. Platt and R. Shack, "History and principles of Shack-Hartmann wavefront sensing," *J. Refract. Surg.* **17**(5), S573–S577 (2001).
7. K. Hampson and M. J. Booth, "Calibration and closed-loop control of deformable mirrors using direct sensing," <https://aomicroscopy.org/dm-calibration-direct-sensing>.
8. E. J. Botcherby, R. Juškaitis, M. J. Booth, and T. Wilson, "An optical technique for remote focusing in microscopy," *Opt. Commun.* **281**(4), 880–887 (2008).
9. K. M. Dean, P. Roudot, C. R. Reis, E. S. Welf, M. Mettlen, and R. Fiolka, "Diagonally scanned light-sheet microscopy for fast volumetric imaging of adherent cells," *Biophys. J.* **110**(6), 1456–1465 (2016).
10. W. J. Shain, N. A. Vickers, B. B. Goldberg, T. Bifano, and J. Mertz, "Extended depth-of-field microscopy with a high-speed deformable mirror," *Opt. Lett.* **42**(5), 995–998 (2017).
11. M. Žurauskas, O. Barnstedt, M. Frade-Rodríguez, S. Waddell, and M. J. Booth, "Rapid adaptive remote focusing microscope for sensing of volumetric neural activity," *Biomed. Opt. Express* **8**(10), 4369–4379 (2017).
12. J. Cui, R. Turcotte, N. J. Emptage, and M. J. Booth, "Extended range and aberration-free autofocusing via remote focusing and sequence-dependent learning," *Opt. Express* **29**(22), 36660–36674 (2021).
13. O. Kafri, "Noncoherent method for mapping phase objects," *Opt. Lett.* **5**(12), 555–557 (1980).
14. J. H. Massig, "Measurement of phase objects by simple means," *Appl. Opt.* **38**(19), 4103–4105 (1999).
15. H. Canabal and J. Alonso, "Automatic wavefront measurement technique using a computer display and a charge-coupled device camera," *Opt. Eng.* **41**(4), 822–826 (2002).
16. I. Trumper, H. Choi, and D. W. Kim, "Instantaneous phase shifting deflectometry," *Opt. Express* **24**(24), 27993–28007 (2016).
17. L. Huang, M. Idir, C. Zuo, and A. Asundi, "Review of phase measuring deflectometry," *Opt. Lasers Eng.* **107**, 247–257 (2018).
18. L. Huang, C. Zhou, W. Zhao, H. Choi, L. Graves, and D. Kim, "Close-loop performance of a high precision deflectometry controlled deformable mirror (DCDM) unit for wavefront correction in adaptive optics system," *Opt. Commun.* **393**, 83–88 (2017).
19. R. J. Noll, "Zernike polynomials and atmospheric turbulence," *J. Opt. Soc. Am.* **66**(3), 207–211 (1976).
20. R. Cubalchini, "Modal wave-front estimation from phase derivative measurements," *J. Opt. Soc. Am.* **69**(7), 972–977 (1979).
21. J. Antonello, "Optimisation-based wavefront sensorless adaptive optics for microscopy," Ph.D. thesis, Delft Univ. Technol. (2014).
22. J. L. Flores, B. Bravo-Medina, and J. A. Ferrari, "One-frame two-dimensional deflectometry for phase retrieval by addition of orthogonal fringe patterns," *Appl. Opt.* **52**(26), 6537–6542 (2013).
23. M. Takeda, H. Ina, and S. Kobayashi, "Fourier-transform method of fringe-pattern analysis for computer-based topography and Interferometry," *J. Opt. Soc. Am.* **72**(1), 156–160 (1982).
24. R. Juškaitis, T. Wilson, M. A. A. Neil, and M. Kozubek, "Efficient real-time confocal microscopy with white light sources," *Nature* **383**(6603), 804–806 (1996).
25. T. Wilson, R. Juškaitis, M. A. A. Neil, and M. Kozubek, "Confocal microscopy by aperture correlation," *Opt. Lett.* **21**(23), 1879–1881 (1996).
26. S. A. Hussain, T. Kubo, N. Hall, D. Gala, K. Hampson, R. Parton, M. A. Phillips, M. Wincott, K. Fujita, I. Davis, I. Dobbie, and M. J. Booth, "Wavefront-sensorless adaptive optics with a laser-free spinning disk confocal microscope," *J. Microsc.* **288**(2), 106–116 (2022).
27. J. Cui, J. Antonello, A. R. Kirkpatrick, P. S. Salter, and M. J. Booth, "Generalised adaptive optics method for high-NA aberration-free refocusing in refractive-index-mismatched media," *Opt. Express* **30**(7), 11809–11824 (2022).
28. M. J. Booth, "Wavefront sensorless adaptive optics for large aberrations," *Opt. Lett.* **32**(1), 5–7 (2007).
29. A. Jesacher and M. J. Booth, "Sensorless adaptive optics for microscopy," *Proc. SPIE* **7931**, 78310G (2011).
30. U. Bitenc, N. A. Bharmal, T. J. Morris, and R. M. Myers, "Assessing the stability of an ALPAO deformable mirror for feed-forward operation," *Opt. Express* **22**(10), 12438–12451 (2014).